Pergamon

Int. J. Solids Structures Vol. 33, No. 26, pp. 3843–3864, 1996

0020-7683/96 $15.00 + .00

0020-7683(95)00217-0

TWO-DIMENSIONAL TIME DOMAIN BEM FOR SCATTERING OF ELASTIC WAVES IN SOLIDS OF GENERAL ANISOTROPY

C.-Y. WANG and J. D. ACHENBACH
Center for Quality Engineering and Failure Prevention, Northwestern University, Evanston, IL 60208-3020, U.S.A.

and

S. HIROSE
Department of Environmental and Civil Engineering, Okayama University, 3-1-1 Tsushima-Naka, Okayama 700, Japan

(*Received* 30 *March* 1995; *in revised form* 13 *September* 1995)

Abstract An efficient two-dimensional time-domain application of the Boundary Element Method is presented to solve elastodynamic boundary initial-value problems in solids of general anisotropy. The method is based on the use of integral expressions for the Green's functions derived by Wang and Achenbach (1994) [Elastodynamic fundamental solutions for anisotropic solids. *Geophys. J. Int.* **118**, 384–392], and on the partition of these Green's functions into singular static and regular dynamic parts. The singular static parts are the elastostatic Green's functions, which have relatively simple explicit expressions in closed form. The regular dynamic parts are given in terms of line integrals over a unit circle, whose integrands have a simple structure which physically corresponds to a superposition of plane waves. The partition of the Green's functions leads to the decomposition of the singular elastodynamic boundary integral equation into terms corresponding to a singular elastostatic integral equation plus regular dynamic terms. The calculation effort is reduced by analytically evaluating both the integration over each boundary element and the time-convolution over each time-step. As a result only regular line integrals over the unit circle have to be computed numerically. Applications are discussed for scattering of elastic waves by cavities. The method has been checked by comparing numerical results against existing analytical solutions for an isotropic solid. Numerical results for scattering of elastic waves in a transversely isotropic material by a circular cylindrical cavity have also been obtained. Copyright © 1996 Elsevier Science Ltd.

1. INTRODUCTION

Many solids are either intrinsically anisotropic, or they are anisotropic on some length scale of the deformation relative to the characteristic length of the structuring of the solid. Examples are the earth, ice, composites, and piezoelectric materials. Elastodynamic boundary/initial-value problems for bodies of anisotropic linearly elastic solids are generally solvable only by numerical techniques. Among these techniques, the reduction of the problem formulation to a boundary integral equation for field variables on the boundary of the body, and the subsequent calculation of these variables by the boundary element method (BEM), has proven to be efficient and accurate. Once the fields on the boundary of the body have been obtained, the fields elsewhere in the solid can be determined by the use of an appropriate elastodynamic representation integral. The method is particularly attractive for scattering analysis in unbounded bodies because only the internal boundaries need to be discretized, and the radiation conditions are satisfied automatically.

For a successful implementation of the BEM, the Green's functions, i.e., the displacement and stress fields in an unbounded solid due to the application of a point force, must be known in relatively simple form since they are the kernel functions in the boundary integral equations and must be computed many times in the process of solving the discretized system of equations. In an isotropic solid explicit expressions for the Green's functions are relatively simple. For two-dimensional (2-D) static problems in anisotropic solids relatively simple explicit expressions for the Green's functions are also available (Barnett and Lothe,

1973; Hwu and Yen, 1991; Stroh, 1958; Ting, 1992; Wang, 1994). Three-dimensional (3-D) static and 2-D time transient Green's functions also have explicit expressions in closed form (Wang, 1995; Wang and Achenbach, 1992), but they are much more complicated. For a solid of general anisotropy, 3-D time-harmonic and time-transient Green's functions, as well as 2-D time-harmonic Green's functions, do not have explicit solutions in closed form. The BEM has been applied to 2-D static problems (Cruse, 1988) and to some three-dimensional (3-D) static problems in anisotropic solids (Vogel and Rizzo, 1973; Wilson and Cruse, 1978; DiNicola, 1994).

In a recent paper of Wang and Achenbach (1994), a method to construct the Green's functions based on the use of the Radon transform has been presented. By this method 3-D and 2-D time-domain elastodynamic Green's functions for linearly elastic anisotropic solids can be obtained in a straightforward manner. The Green's functions in the frequency-domain follow directly by an evaluation of the Fourier transforms of the time domain solutions. The solutions are in the form of a surface integral over a unit sphere for 3-D cases and a contour integral over a unit circle for 2-D cases. The integrals have a simple structure which is very attractive for practical applications, especially when integrations and differentiations must be carried out. In this paper, we present a novel BEM approach using these integral expressions for the Green's functions. This approach is applicable to 2-D and 3-D elastodynamic problems in both time-domain and frequency domain, but the material presented in this paper is concerned with 2-D time-domain problems.

Even though 2-D time-domain Green's functions have explicit solutions in closed form, we choose to use the integral expressions for the Green's functions because they are easier to use. The structure of the integral expressions simplifies the BEM formulations. The numerical computations then reduce to an extent that the computational time for general anisotropy is close to or even less than that required by conventional BEM for isotropic materials.

The first important step is the decomposition of the Green's functions into singular static and regular dynamic parts. This decomposition separates the singular elastodynamic boundary integral equation into a singular elastostatic integral equation plus regular dynamic terms. The singular parts of the Green's functions correspond to the elastostatic Green's functions in anisotropic solids. The regular dynamic parts are given in terms of line integrals over a unit circle, whose integrands have a simple structure which physically correspond to a superposition of plane waves. The second important step is to analytically evaluate the integration over each boundary element as well as the time-convolution over each time-step. As a result, the only numerical computations are regular line integrals over the unit circle.

The present work provides a powerful numerical technique to solve boundary/initial-value problems in general anisotropic solids. The method has been demonstrated by checking numerical results against existing analytical solutions for an isotropic solid. Numerical results for scattering of acoustic waves by a cylindrical cavity in a transversely isotropic material are also presented.

2. STATEMENT OF THE PROBLEM

2.1. *Basic equations*

We consider a 2-D elastodynamic boundary/initial-value problem in a homogeneous anisotropic linearly elastic solid, and we define a fixed rectangular coordinate system, x_i, so that the 2-D problem is stated in the (x_1, x_2)-plane and the field quantities are independent of x_3. The fields are governed by the equations of motion and the stress-displacement relations, given by

$$\sigma_{i\alpha,\alpha}(\mathbf{x}, t) + \rho \ddot{u}_i(\mathbf{x}, t) = 0, \tag{1}$$

$$\sigma_{i\alpha}(\mathbf{x}, t) = c_{i\alpha j\beta} u_{j,\beta}(\mathbf{x}, t) \tag{2}$$

where u_i and $\sigma_{i\alpha}$ are the displacement and stress components, ρ is the mass density, and c_{ijpq}

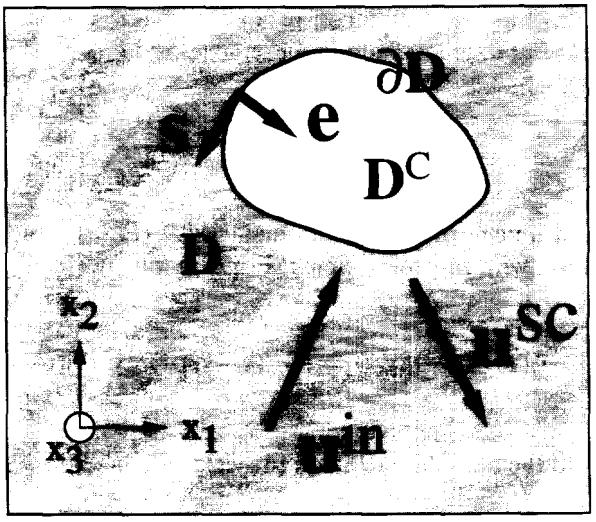

Fig. 1. Geometry of the problem.

is the tensor of elastic moduli. Substitution of (2) into (1) leads to the partial differential equations

$$\{\Gamma_{ij}(\hat{c}_1, \hat{c}_2) - \rho \hat{c}_1^2 \delta_{ij}\} u_j(\mathbf{x}, t) = 0 \tag{3}$$

where

$$\Gamma_{ij}(\hat{c}_1, \hat{c}_2) = c_{i\alpha j\beta} \hat{c}_\alpha \hat{c}_\beta. \tag{4}$$

Note that eqn (3) corresponds to a set of three coupled equations. Antiplane and inplane motions generally do not uncouple in anisotropic solids.

Throughout this paper, a Roman suffix takes the values of 1, 2 and 3, while a Greek suffix takes the values of 1 and 2 only. The summation convention is applied over the range of the suffixes. Bold-face letters are used to denote 2-D vectors, e.g., $\mathbf{x}$ has components x_α, and $\mathbf{s} \cdot \mathbf{x} = s_\alpha x_\alpha$. For a function $f(\mathbf{x}, t)$, we denote the derivatives with respect to x_α by $\hat{c}_\alpha f$ or $f_{,\alpha}$; and the derivatives with respect to time t by $\hat{c}_t f$ or $\dot{f}$.

2.2. *Boundary integral equations for scattering of elastic waves*

We are interested in scattering of elastic waves in anisotropic solids. Particularly we shall consider a cavity D^C in an unbounded anisotropic solid D subjected to an incident wave u_i^{in} (see Fig. 1). The solid is at rest before the application of the incident wave. When the incident wave reaches the cavity, a scattered wave field u_i^{sc} is generated in order to satisfy prescribed boundary conditions on the surface of the cavity, ∂D. The complete displacement wave field is then given by

$$u_i = u_i^{in} + u_i^{sc}. \tag{5}$$

For this elastodynamic boundary value problem, the usual time-domain integral representation in terms of the displacement u_i and traction t_i on the boundary ∂D is given by (Achenbach, 1972)

$$u_j(\mathbf{x}, t) = u_j^{in}(\mathbf{x}, t) + \int_{\partial D} g_{ij}(\mathbf{y} - \mathbf{x}, t) * t_i(\mathbf{y}, t)\, d\mathbf{y} - \int_{\partial D} h_{ij}[\mathbf{y} - \mathbf{x}, t; \mathbf{e}(\mathbf{y})] * u_i(\mathbf{y}, t)\, d\mathbf{y} \quad \mathbf{x} \in D \tag{6}$$

where $\mathbf{x}$ and $\mathbf{y}$ are usually referred to as the source point and the field point, respectively. In eqn (6) $g_{ij}(\mathbf{x}, t)$ is the elastodynamic displacement Green's function which corresponds

to the displacement field in the x_i-direction produced by an impulsive line load acting in the x_j-direction, applied at time $t = 0$ along the x_3-axis, and $h_{ij}[\mathbf{x}, t; \mathbf{e}]$ is the corresponding traction defined by

$$h_{ij}(\mathbf{x}, t; \mathbf{e}) = c_{i\alpha p\beta} e_\alpha g_{pj,\beta}(\mathbf{x}, t). \tag{7}$$

Here $\mathbf{e}$ is the outward unit normal to the boundary ∂D (Fig. 1). In eqn (6) the asterisk denotes the convolution with respect to time t. For example,

$$g_{ij}(\mathbf{y}-\mathbf{x}, t)*t_i(\mathbf{y}, t) = \int_0^t g_{ij}(\mathbf{y}-\mathbf{x}, t-\tau) t_i(\mathbf{y}, \tau)\, \mathrm{d}\tau.$$

When $\mathbf{x} \in D$ is taken to the boundary ∂D, eqn (6) yields the boundary integral equation:

$$c_{ij}(\mathbf{x}) u_i(\mathbf{x}, t) = u_i^{in}(\mathbf{x}, t) + \int_{\partial D} g_{ij}(\mathbf{y}-\mathbf{x}, t)*t_i(\mathbf{y}, t)\, \mathrm{d}\mathbf{y} - PV \int_{\partial D} h_{ij}[\mathbf{y}-\mathbf{x}, t; \mathbf{e}(\mathbf{y})]*u_i(\mathbf{y}, t)\, \mathrm{d}\mathbf{y}$$

$$\mathbf{x} \in \partial D \tag{8}$$

where PV stands for the principal value of the integral and $c_{ij}(\mathbf{x})$ defines the free terms resulting from the contribution of $h_{ij}[\mathbf{y}-\mathbf{x}, t; \mathbf{e}(\mathbf{y})]$ as $\mathbf{x} \to \mathbf{y}$. Calculations for $c_{ij}(\mathbf{x})$ will be given in Section 3.4.

Let us choose a time axis such that the incident wave reaches the cavity at time $t = 0$. Thus, for $t < 0$, $u_i^{in}(\mathbf{x}, t) = u_i(\mathbf{x}, t) = t_i(\mathbf{x}, t) \equiv 0$ on $\mathbf{x} \in \partial D$. For such zero initial conditions eqn (8) yields unique and stable solutions for $u_i(\mathbf{x}, t)$ and/or $t_i(\mathbf{x}, t)$ on $\mathbf{x} \in \partial D$, for appropriately prescribed boundary conditions. For boundary-value problems of the first kind the prescribed boundary conditions are given by $t_i(\mathbf{x}, t)$ on $\mathbf{x} \in \partial D$, while for boundary-value problems of the second kind they are $u_i(\mathbf{x}, t)$ on $\mathbf{x} \in \partial D$. For mixed boundary-value problems, $t_i(\mathbf{x}, t)$ are given on part of the boundary, while on the remaining part of the boundary $u_i(\mathbf{x}, t)$ are given. Once $u_i(\mathbf{x}, t)$ and $t_i(\mathbf{x}, t)$ on the boundary $\mathbf{x} \in \partial D$ are obtained from eqn (8), the complete fields in the domain D can be determined by eqn (6).

3. GREEN'S FUNCTIONS AND SINGULAR AND REGULAR PARTS

3.1. *Green's functions*

The integral expressions for g_{ij} and h_{ij} derived by Wang and Achenbach (1994) are given by

$$g_{ij}(\mathbf{x}, t) = \frac{H(t)}{4\pi^2} \int_{|\mathbf{n}|=1} \sum_{m=1}^{M} \frac{P_{ij}^m}{\rho c_m} \frac{\mathrm{d}\mathbf{n}}{c_m t + \mathbf{n}\cdot\mathbf{x}} \tag{9}$$

$$h_{ij}(\mathbf{x}, t; \mathbf{e}) = \frac{H(t)}{4\pi^2} \partial t \int_{|\mathbf{n}|=1} \sum_{m=1}^{M} \frac{Q_{ij}^m}{\rho c_m^2} \frac{\mathrm{d}\mathbf{n}}{c_m t + \mathbf{n}\cdot\mathbf{x}} \tag{10}$$

where $H(t)$ denotes the Heaviside step function, $[\rho c_m^2(\mathbf{n})]$ and $P_{ij}^m(\mathbf{n})$ are the eigenvalues and the projection operators for the matrix

$$\Gamma_{ij}(\mathbf{n}) = \Gamma_{ij}(n_1, n_2) = c_{i\alpha j\beta} n_\alpha n_\beta \tag{11}$$

and

$$Q_{ij}^{m}(\mathbf{n},\mathbf{e}) = c_{ixp\beta}e_{\chi}n_{\beta}P_{pj}^{m}(\mathbf{n}). \tag{12}$$

In eqns (9) and (10), M ($1 \leqslant M \leqslant 3$) is the number of distinct eigenvalues $[\rho c_m^2(\mathbf{n})]$ determined by the characteristic equation:

$$\det\left[\Gamma_{ij}(\mathbf{n}) - \rho c_m^2 \delta_{ij}\right] = 0. \tag{13}$$

Equation (13) is a cubic polynomial for $[\rho c_m^2(\mathbf{n})]$. It determines three positive real-valued c_m. If all c_m are distinct, i.e., $c_1 \neq c_2 \neq c_3$ ($M = 3$), $P_{ij}^{m}(\mathbf{n})$ are given by

$$P_{ij}^{m} = \frac{E_{ij}^{m}}{E_{qq}^{m}} \tag{14}$$

where

$$E_{ij}^{m} \equiv \operatorname{adj}\left\{\Gamma_{ij}(\mathbf{n}) - \rho c_m^2 \delta_{ij}\right\}. \tag{15}$$

When $c_1 \neq c_2 = c_3$ ($M = 2$), P_{ij}^{1} is also given by (14) but $P_{ij}^{2} = \delta_{ij} - P_{ij}^{1}$. When $c_1 = c_2 = c_3$ ($M = 1$), $P_{ij}^{1} = \delta_{ij}$.

It is worth noting that the integrals (9) and (10) are defined over the unit circle $|\mathbf{n}| = 1$ and the integrands correspond to plane waves (functions of $c_m t + \mathbf{n}\cdot\mathbf{x}$) propagating in the direction $-\mathbf{n}$. The simple structure of superposed plane waves is fundamental in the derivations throughout this paper.

3.2. *Singular static and regular dynamic parts*

Consider the time-convolution of the Green's functions with a sufficiently smooth function $f(t)$ with $f(t) \equiv 0$ for $t < 0$. By integration by parts we obtain (Wang and Achenbach, 1994).

$$g_{ij}(\mathbf{x},t) * f(t) = g_{ij}^{R}(\mathbf{x},t) * \dot{f}(t) + g_{ij}^{S}(\mathbf{x}) f(t) \tag{16}$$

$$h_{ij}(\mathbf{x},t;\mathbf{e}) * f(t) = h_{ij}^{R}(\mathbf{x},t;\mathbf{e}) * \ddot{f}(t) + h_{ij}^{S}(\mathbf{x};\mathbf{e}) f(t) \tag{17}$$

where $g_{ij}^{R}(\mathbf{x},t)$ and $h_{ij}^{R}(\mathbf{x},t;\mathbf{e})$ are time-dependent regular functions, while $g_{ij}^{S}(\mathbf{x})$ and $h_{ij}^{S}(\mathbf{x};\mathbf{e})$ are time-independent singular functions.

The regular dynamic parts are given by (Wang and Achenbach, 1994)

$$g_{ij}^{R}(\mathbf{x},t) = \frac{H(t)}{4\pi^2} \int_{|\mathbf{n}|=1} \sum_{m=1}^{M} \frac{P_{ij}^{m}}{\rho c_m^2} \log|c_m t + \mathbf{n}\cdot\mathbf{x}|\, \mathrm{d}\mathbf{n}. \tag{18}$$

and

$$h_{ij}^{R}(\mathbf{x},t;\mathbf{e}) = \frac{H(t)}{4\pi^2} \int_{|\mathbf{n}|=1} \sum_{m=1}^{M} \frac{Q_{ij}^{m}}{\rho c_m^3} \log|c_m t + \mathbf{n}\cdot\mathbf{x}|\, \mathrm{d}\mathbf{n}. \tag{19}$$

The static singular parts $g_{ij}^{S}(\mathbf{x})$ and $h_{ij}^{S}(\mathbf{x};\mathbf{e})$ can be reduced to relatively simple closed form expressions. In eqn (16), $g_{ij}^{S}(\mathbf{x})$ is given by (Wang and Achenbach, 1994)

$$g_{ij}^{S}(\mathbf{x}) = \frac{-1}{4\pi^2} \int_{|\mathbf{n}|=1} \Gamma_{ij}^{-1}(\mathbf{n}) \log|\mathbf{n}\cdot\mathbf{x}|\, \mathrm{d}\mathbf{n}.$$

For positions ahead of the wavefront, eqn (18) reduces to time independent fields which just cancel the static singular parts. Now, introducing $\eta = n_2/n_1$, we have

$$g_{ij}^S(\mathbf{x}) = \frac{-1}{2\pi^2}\int_{-\infty}^{\infty} \frac{A_{ij}(\eta)}{D(\eta)} \log|x_1 + \eta x_2|\, d\eta + C_{ij} \tag{20}$$

where C_{ij} are constants given by

$$C_{ij} = \frac{-1}{4\pi^2}\int_{|\mathbf{n}|=1} \Gamma_{ij}^{-1}(\mathbf{n}) \log|n_1|\, d\mathbf{n} \tag{21}$$

and

$$A_{ij}(\eta) = \text{adj}\,[\Gamma_{ij}(1,\eta)], \quad D(\eta) = \det[\Gamma_{ij}(1,\eta)]. \tag{22}$$

Application of the residue calculus to the integral in eqn (20) yields (Wang, 1994)

$$g_{ij}^S(\mathbf{x}) = \frac{1}{\pi}\text{Im}\sum_{m=1}^{3}\left[\frac{A_{ij}(\eta_m)}{\hat{c}_\eta D(\eta_m)} \log(z_m)\right] + C_{ij} \tag{23}$$

where

$$z_m = x_1 + \eta_m x_2, \tag{24}$$

and η_m are the roots with $\text{Im}\,(\eta_m) > 0$ $(m = 1, 2, 3)$ of

$$D(\eta_m) = 0. \tag{25}$$

We note that $g_{ij}^S(\mathbf{x})$ given by eqn (23) corresponds to the elastostatic Green's functions for anisotropic solids obtained by Wang (1994). The constants C_{ij} are inessential in the elastostatic Green's functions, but they are required here to maintain the quiescent field ahead of the wavefronts generated by the line force. It is interesting to note the similarity of eqn (23) with $\log(z)$ $(z = x_1 + ix_2)$, the Green's function of Laplace's equation. Equation (23) will be used later to analytically evaluate integrations over the boundary elements.

Next we present some details that are useful in the numerical evaluation of $g_{ij}^S(\mathbf{x})$. According to (11), we may write

$$\Gamma_{ij}(1,\eta) = L_{ij}\eta^2 + (M_{ij} + M_{ij}^T)\eta + N_{ij} \tag{26}$$

where

$$L_{ij} = c_{2ij2}, \quad M_{ij} = c_{2ij1}, \quad N_{ij} = c_{1ij1}, \tag{27}$$

and M_{ij}^T is the transpose of M_{ij}. Since $D(\eta)$ is a polynomial of order six with real-valued coefficients, it has three roots at η_m defined by eqn (25) and three roots at $\bar{\eta}_m$. Thus

$$D(\eta) = \sum_{k=0}^{6} a_k \eta^k = a_6 \sum_{m=1}^{3} (\eta - \eta_m)(\eta - \bar{\eta}_m) \tag{28}$$

where $\bar{\eta}_m$ are the conjugates of η_m and a_k are the coefficients of the polynomial $D(\eta)$. From eqns (22) and (26), it is easy to conclude that

$$a_6 = \det[L_{pk}]. \tag{29}$$

As a consequence of eqn (28), we have

$$\partial_\eta D(\eta_m) = [D(\eta)/(\eta-\eta_m)] \quad \text{at } \eta = \eta_m. \tag{30}$$

It is expedient to give $h_{ij}^S(\mathbf{x};\mathbf{e})$ in terms of a traction potential $\Phi_{ij}(\mathbf{x})$ as (Ting, 1992)

$$h_{ij}^S(\mathbf{x},\mathbf{e}) = \partial_{\mathbf{s}}\Phi_{ij}(\mathbf{x}) \tag{31}$$

where $\partial_{\mathbf{s}} = s_1\partial_1 + s_2\partial_2$ is the differential in the direction $\mathbf{s}$, with $\mathbf{s}$ being the unit tangent vector of the boundary ∂D. Thus $\mathbf{s}\cdot\mathbf{e} = 0$. In the coordinate system shown in Fig. 1, $s_1 = e_2$ and $s_2 = -e_1$. The traction potential is given by

$$\Phi_{ij}(\mathbf{x}) = \frac{1}{\pi}\operatorname{Im}\sum_{m=1}^{3}\left[\frac{B_{ij}(\eta_m)}{\partial_\eta D(\eta_m)}\log(z_m)\right] \tag{32}$$

where

$$B_{ij}(\eta) = (L_{ip}\eta + M_{ip})A_{pj}(\eta). \tag{33}$$

According to eqns (22) and (26), $B_{ij}(\eta)$ can be written as

$$B_{ij}(\eta) = b_{ij}^5\eta^5 + b_{ij}^4\eta^4 + \cdots + b_{ij}^0 \tag{34}$$

where b_{ij}^k ($k = 0$–5) are the coefficients of the polynomials $B_{ij}(\eta)$. Specifically

$$b_{ij}^5 = L_{ip}\operatorname{adj}[L_{pj}] = \det[L_{pq}]\delta_{ij} = a_6\delta_{ij}. \tag{35}$$

The results of eqns (34) and (35) will be used later to calculate the free term c_{ij}.

Up to now we have assumed that η_m are distinct roots of eqn (25). For certain materials, e.g., isotropic solids, η_m are not all distinct. For such cases, we say that the solid is degenerated. For degenerated solids the solutions for $g_{ij}^S(\mathbf{x})$ and $\Phi_{ij}(\mathbf{x})$ given by eqns (23) and (32) must be modified since the denominator $\partial_\eta D(\eta_m) = 0$. Degenerated solids have been discussed by Wang (1994). In practical numerical computations, however, satisfactory results can be obtained by slightly changing the elastic constants c_{ijpq} so that all η_m become distinct. Finally we remark that although $\log(z_m)$ is multi-valued, $g_{ij}^S(\mathbf{x})$ and $\Phi_{ij}(\mathbf{x})$ given by eqns (23) and (32) are single-valued as they should be.

3.3. *Decomposition of the boundary integral equations*

Substitution of eqns (16) and (17) into (6) leads to

$$\begin{aligned} u_i(\mathbf{x},t) = u_i^{in}(\mathbf{x},t) &+ \int_{\partial D} g_{ij}^S(\mathbf{y}-\mathbf{x})t_j(\mathbf{y},t)\,d\mathbf{y} - \int_{\partial D} h_{ij}^S[\mathbf{y}-\mathbf{x};\mathbf{e}(\mathbf{y})]u_j(\mathbf{y},t)\,d\mathbf{y} \\ &+ \int_{\partial D} g_{ij}^R(\mathbf{y}-\mathbf{x},t)*t_j(\mathbf{y},t)\,d\mathbf{y} - \int_{\partial D} h_{ij}^R[\mathbf{y}-\mathbf{x},t;\mathbf{e}(\mathbf{y})]*\ddot{u}_j(\mathbf{y},t)\,d\mathbf{y}, \quad \mathbf{x}\in D \end{aligned} \tag{36}$$

which, when $\mathbf{x}\in D$ approaches to the boundary ∂D, yields

$$\begin{aligned} c_{ij}(\mathbf{x})u_j(\mathbf{x},t) = u_i^{in}(\mathbf{x},t) &+ \int_{\partial D} g_{ij}^S(\mathbf{y}-\mathbf{x})t_j(\mathbf{y},t)\,d\mathbf{y} - PV\int_{\partial D} h_{ij}^S[\mathbf{y}-\mathbf{x};\mathbf{e}(\mathbf{y})]u_j(\mathbf{y},t)\,d\mathbf{y} \\ &+ \int_{\partial D} g_{ij}^R(\mathbf{y}-\mathbf{x},t)*t_j(\mathbf{y},t)\,d\mathbf{y} - \int_{\partial D} h_{ij}^R[\mathbf{y}-\mathbf{x},t;\mathbf{e}(\mathbf{y})]*\ddot{u}_j(\mathbf{y},t)\,d\mathbf{y}, \quad \mathbf{x}\in\partial D. \end{aligned} \tag{37}$$

We note that the time convolutions involve only the regular dynamic terms g_{ij}^R and h_{ij}^R. Without the last two terms, eqn (37) corresponds to the boundary integral equation for

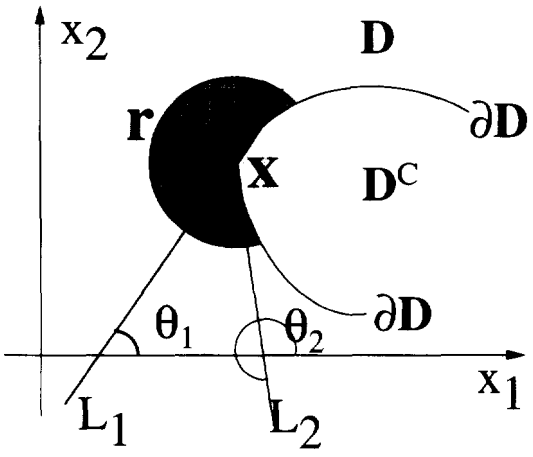

Fig. 2. Geometry for the free term c_{ij}.

an elastostatic problem. The calculation of the singular dynamic integrals is thus simplified to the evaluation of singular static integrals and regular dynamic integrals.

3.4. *The free term* c_{ij}

Equation (37) also shows that the free term $c_{ij}(\mathbf{x})$ comes from the singularity of $h_{ij}^S[\mathbf{y}-\mathbf{x};\mathbf{e}(\mathbf{y})]$ as $\mathbf{x}\to\mathbf{y}$ and has nothing to do with h_{ij}^R. There are many ways to evaluate $c_{ij}(\mathbf{x})$. Here we follow the approach commonly used in the BEM for isotropic solids.

Assume that the boundary curve ∂D is not "smooth" at $\mathbf{x}$, meaning that the two tangents approaching $\mathbf{x}$ from different sides do not coincide (see Fig. 2, where L_1 and L_2 denote these two tangent lines). The free term may then be defined by

$$c_{ij}(\mathbf{x}) = \lim_{r\to 0}\int_{\theta_1}^{\theta_2} h_{ij}^S[\mathbf{r};\mathbf{e}]r\,\mathrm{d}\theta \quad \text{with} \quad r=|\mathbf{r}| \quad \text{and} \quad \mathbf{e}=-\mathbf{r}/r \tag{38}$$

where θ is the angle between $\mathbf{r}$ and the x_1-axis. The geometry of $\mathbf{r}(\theta)$, θ_1 and θ_2 is indicated in Fig. 2. As shown in Fig. 2, $\mathbf{r}(\theta)$ defines a circle centered at $\mathbf{x}$ with radius r. In eqn (38) the integral is defined along the part of the circle that is inside the domain D. Substitution of eqn (31) into eqn (38) yields

$$\begin{aligned} c_{ij} &= \lim_{r\to 0}\int_{\theta_1}^{\theta_2} \hat{c}_s\Phi_{ij}(\mathbf{r})r\,\mathrm{d}\theta = \lim_{r\to 0}\{\Phi_{ij}[\mathbf{r}(\theta_2)]-\Phi_{ij}[\mathbf{r}(\theta_1)]\} \\ &= \frac{1}{\pi}\,\mathrm{Im}\sum_{m=1}^{3}\left\{\frac{B_{ij}(\eta_m)}{\hat{c}_\eta D(\eta_m)}\log\left[\frac{\cos\theta_2+\eta_m\sin\theta_2}{\cos\theta_1+\eta_m\sin\theta_1}\right]\right\} \end{aligned} \tag{39}$$

Here, $\hat{c}_s = (1/r)\hat{c}_\theta$ and eqn (32) has been used.

If the boundary is smooth at $\mathbf{x}$, then $\theta_2=\theta_1+\pi$ and eqn (39) reduces to

$$c_{ij} = \mathrm{Re}\sum_{m=1}^{3}\frac{B_{ij}(\eta_m)}{\hat{c}_\eta D(\eta_m)}. \tag{40}$$

This result can be simplified by observing that

$$\int_C \frac{B_{ij}(\eta)}{D(\eta)}\,\mathrm{d}\eta = 2\pi i \sum_{m=1}^{3}\left[\frac{B_{ij}(\eta_m)}{\hat{c}_\eta D(\eta_m)} + \frac{B_{ij}(\bar{\eta}_m)}{\hat{c}_\eta D(\bar{\eta}_m)}\right] = 2\pi i\,\mathrm{Re}\sum_{m=1}^{3}\frac{2B_{ij}(\eta_m)}{\hat{c}_\eta D(\eta_m)} \tag{41}$$

where C is a closed contour in the complex η-plane enclosing all the poles at η_m and $\bar{\eta}_m$. On the other hand, we also have

$$\int_C \frac{B_{ij}(\eta)}{D(\eta)}\,\mathrm{d}\eta = \lim_{|\eta|\to\infty}\int_0^{2\pi}\frac{B_{ij}(|\eta|e^{i\theta})}{D(|\eta|e^{i\theta})}(i|\eta|e^{i\theta})\,\mathrm{d}\theta = 2\pi i\delta_{ij}. \tag{42}$$

The last equality is obtained by using eqns (28), (29), (34) and (35) and by taking the limit. Comparison of eqns (40), (41) and (42) reveals that

$$c_{ij} = \tfrac{1}{2}\delta_{ij} \tag{43}$$

which agrees with the well-known result for an isotropic solid.

This agreement is not at all surprising. As a matter of fact, the result of eqn (43) can also be obtained based on simple physical arguments. As we know, h_{ij}^S corresponds to the traction produced by a static line force of unit amplitude in the direction x_j. Thus, c_{ij} defined by the integral (38) has the physical meaning of the force resultant from the integration of the traction over part of a circle around the line force. If the integration is carried out over the complete circle, we should have $c_{ij} = \delta_{ij}$ because the overall traction must balance the line force. On the other hand, referring to Fig. 2, since

$$h_{ij}^S[-\mathbf{r}; -\mathbf{e}] = h_{ij}^S[\mathbf{r}; \mathbf{e}] \tag{44}$$

the integration over half of the circle must equal half of that over the complete circle. Hence, we have eqn (43). Equation (44) can be verified from either eqn (31) or observations on the symmetry of the problem. We note that eqn (44) depends only on the symmetry in a homogenous space. The result of eqn (43) should be universal for a smooth boundary in any kind of homogenous material.

4. NUMERICAL IMPLEMENTATION

4.1. *Time-stepping technique of time-domain BEM*

The basic idea of the BEM is to approximate the fields on the boundary by their values at a finite number of points and at a finite number of times along the time axis. In doing so, the boundary integral eqn (37) is replaced by a finite system of linear algebraic equations that can be solved numerically. The approximation is achieved by using shape functions. In this section the basic steps of the conventional time-stepping technique of the time-domain BEM (Kitahara, Hirose and Achenbach, 1992; Manolis and Beskos, 1988; Wang and Takemiya, 1992) are briefly reviewed.

Let us choose N points $\mathbf{x} = \mathbf{x}_n$ ($n = 1$–N) on the boundary $\mathbf{x}_n \in \partial D$ and K points $t = t^k$ ($k = 1$–K) along the time axis. For simplicity of notation, let

$$[u_i^{nk}, t_i^{nk}, u_i^{in,nk}, c_{ij}^n] = [u_i(\mathbf{x}, t), t_i(\mathbf{x}, t), u_i^{in}(\mathbf{x}, t), c_{ij}(\mathbf{x})] \quad \text{at} \quad (\mathbf{x} = \mathbf{x}_n, t = t^k). \tag{45}$$

The fields on the boundary are approximated by

$$u_i(\mathbf{x}, t) \approx \sum_{n=1}^{N}\sum_{k=1}^{K}\phi_u^n(\mathbf{x})\varphi_u^k(t)u_i^{nk}, \quad \text{and} \quad t_i(\mathbf{x}, t) \approx \sum_{n=1}^{N}\sum_{k=1}^{K}\phi_t^n(\mathbf{x})\varphi_t^k(t)t_i^{nk} \tag{46}$$

where $\phi_u^n(\mathbf{x})$ and $\phi_t^n(\mathbf{x})$ are the spatial shape functions associated with $\mathbf{x}_n$, and $\varphi_u^k(t)$ and $\varphi_t^k(t)$ are the temporal shape functions associated with t^k. The subscripts u and t indicate the correspondence to the displacement u_i and traction t_i respectively. Note that in this

section and in the sequel, the summation convention applies to the subscript j only. As usual, we require

$$\phi_u^n(\mathbf{x}_m) = \phi_t^n(\mathbf{x}_m) = \delta_{mn} \quad \text{and} \quad \varphi_u^k(t^K) = \varphi_t^k(t^K) = \delta_{kK}. \tag{47}$$

The computation for the time-convolution can be reduced significantly if the time axis is divided into equal increments Δt (thus, $t^k = k\Delta t$) and if the temporal shape functions are chosen such that

$$\varphi_u^k(t) = \varphi_u(t-t^{k-1})H(t-t^{k-1}) \quad \text{and} \quad \varphi_t^k(t) = \varphi_t(t-t^{k-1})H(t-t^{k-1}). \tag{48}$$

Equation (48) means that the temporal shape functions have the same shape for different time-steps, and that the current events at $t = t^k$ do not influence previous events at $t \leqslant t^{k-1}$.

Substitution of eqns (45) $\sim$ (48) into eqn (37) leads to

$$c_{ij}^m u_i^{mK} = u_j^{in,mK} + \sum_{n=1}^{N} [G_{ij}^S(m,n)t_i^{nK} - H_{ij}^S(m,n)u_i^{nK}] + \sum_{k=1}^{K}\sum_{n=1}^{N} [G_{ij}^R(m,n;K-k+1)t_i^{nk} - H_{ij}^R(m,n;K-k+1)u_i^{nk}] \tag{49}$$

where

$$G_{ij}^S(m,n) = \int_{\partial D} g_{ij}^S[\mathbf{y}-\mathbf{x}]\phi_t^n(\mathbf{y})\,\mathrm{d}\mathbf{y} \quad \text{at} \quad (\mathbf{x} = \mathbf{x}_m) \tag{50a}$$

$$H_{ij}^S(m,n) = \int_{\partial D} h_{ij}^S[\mathbf{y}-\mathbf{x};\mathbf{e}(\mathbf{y})]\phi_u^n(\mathbf{y})\,\mathrm{d}\mathbf{y} \quad \text{at} \quad (\mathbf{x} = \mathbf{x}_m) \tag{50b}$$

$$G_{ij}^R(m,n;k) = \int_{\partial D} g_{ij}^R[\mathbf{y}-\mathbf{x},t]^*\dot{\varphi}_t(t)\phi_t^n(\mathbf{y})\,\mathrm{d}\mathbf{y} \quad \text{at} \quad (\mathbf{x} = \mathbf{x}_m, t = t^k) \tag{51a}$$

$$H_{ij}^R(m,n;k) = \int_{\partial D} h_{ij}^R[\mathbf{y}-\mathbf{x},t;\mathbf{e}(\mathbf{y})]^*\ddot{\varphi}_u(t)\phi_u^n(\mathbf{y})\,\mathrm{d}\mathbf{y} \quad \text{at} \quad (\mathbf{x} = \mathbf{x}_m, t = t^k). \tag{51b}$$

Equation (49) can be written in matrix form as

$$\mathbf{C}\mathbf{U}_K = \mathbf{U}_K^{in} + \mathbf{G}^S\mathbf{T}_K - \mathbf{H}^S\mathbf{U}_K + \sum_{k=1}^{K} [\mathbf{G}_{K-k+1}^R\mathbf{T}_k - \mathbf{H}_{K-k+1}^R\mathbf{U}_k] \tag{52}$$

where, for a fixed k, $\mathbf{U}_k$, $\mathbf{T}_k$ and $\mathbf{U}_k^{in}$ are $3N$ vectors corresponding to $u_i(\mathbf{x}_n, t^k)$, $t_i(\mathbf{x}_n, t^k)$ and $u_i^{in}(\mathbf{x}_n, t^k)$, respectively (e.g. the $3N$ vector $\mathbf{U}_k$ is constructed from $u_i(\mathbf{x}_n, t^k)$ as i is 1, 2 or 3, while for each i, n runs from 1 to N). The $3N \times 3N$ matrices $\mathbf{C}$, $\mathbf{G}^S$, $\mathbf{H}^S$, $\mathbf{G}_k^R$ and $\mathbf{H}_k^R$ are similarly constructed.

We may put eqn (52) into the following form:

$$\mathbf{H}\mathbf{U}_K = \mathbf{G}\mathbf{T}_K + \mathbf{F}_K \tag{53}$$

where

$$\mathbf{H} = \mathbf{C} + \mathbf{H}^S + \mathbf{H}_1^R, \quad \mathbf{G} = \mathbf{G}^S + \mathbf{G}_1^R \tag{54}$$

and

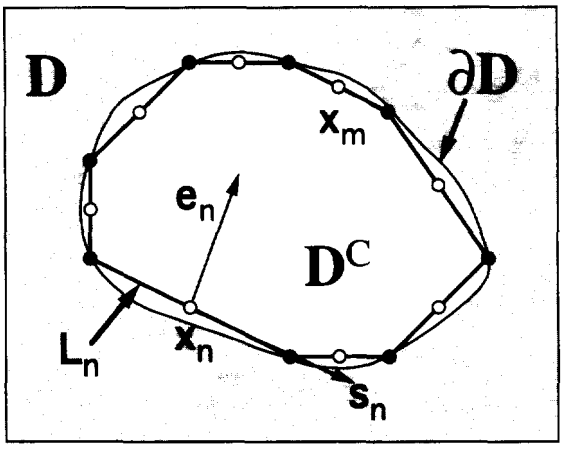

Fig. 3. Elements on discretized boundary.

$$\mathbf{F}_K = \mathbf{U}_K^m + \sum_{k=1}^{K-1} [\mathbf{G}_{K-k+1}^R \mathbf{T}_k - \mathbf{H}_{K-k+1}^R \mathbf{U}_k]. \tag{55}$$

We note that $\mathbf{F}_K$ consists of the incident wave term and the accumulated effects of previous responses. For simplicity of explanation, let us consider a boundary-value problem of the first kind where $\mathbf{T}_K$ are the prescribed boundary conditions. If $\mathbf{F}_K$ is known at time $t = t^K$ we can determine $\mathbf{U}_K$ from eqn (53) simply by an inversion of $\mathbf{H}$. We start from $K = 1$ where $\mathbf{F}_K = \mathbf{U}_K^m$ and thus $\mathbf{U}_K$ can be determined. These solutions will then be used to determine $\mathbf{F}_{K+1}$ for the next time-step by eqn (55), and subsequently to calculate $\mathbf{U}_{K+1}$ by eqn (53). Repeating the procedure in this way, one time-step after another, solutions along the time axis can be computed.

4.2. *Evaluation of* $\boldsymbol{G}^S$ *and* $\boldsymbol{H}^S$

From eqn (53) it can be seen that the essential part of the time-domain BEM is the computation of the matrices $\mathbf{G}^S$, $\mathbf{H}^S$, $\mathbf{G}_k^R$ and $\mathbf{H}_k^R$. In this section we derive closed form solutions for $G_{ij}^S(m,n)$ and $H_{ij}^S(m,n)$ defined by eqn (50). To carry out the integrations in a practically efficient way, the boundary is usually discretized into "elements" and the spatial shape functions are defined locally. Here, we consider the simplest case of straight line elements and constant spatial shape functions, although the method works as well for curved elements and higher ordered shape functions.

We approximate the boundary by straight line elements L_n ($n = 1$–N) as shown in Fig. 3. Thus

$$\partial D \approx \sum_{n=1}^{N} L_n. \tag{56}$$

Let $\mathbf{x}_n$ be taken at the center of L_n and let us choose constant shape functions as

$$\phi_u^n(\mathbf{x}) = \phi_t^n(\mathbf{x}) = \begin{cases} 1 & \text{if } \mathbf{x} \in L_n \\ 0 & \text{otherwise} \end{cases} \tag{57}$$

Then, $G_{ij}^S(m,n)$ and $H_{ij}^S(m,n)$ defined by eqn (50) can be written as

$$[G_{ij}^S(m,n), H_{ij}^S(m,n)] = [V_{ij}^S(\mathbf{x};\mathbf{s},a), W_{ij}^S(\mathbf{x};\mathbf{s},a)] \quad \text{at} \quad (\mathbf{x} = \mathbf{x}_n - \mathbf{x}_m, \mathbf{s} = \mathbf{s}_n, a = a_n) \tag{58}$$

where

$$V_{ij}^S(\mathbf{x};\mathbf{s},a)=\int_{-a}^{a} g_{ij}^S(\mathbf{x}+\mathbf{s}\xi)\,\mathrm{d}\xi,\quad W_{ij}^S(\mathbf{x};\mathbf{s},a)=\int_{-a}^{a} h_{ij}^S(\mathbf{x}+\mathbf{s}\xi;\mathbf{e})\,\mathrm{d}\xi \tag{59}$$

and $\mathbf{s}_n$ and $2a_n$ are the unit tangent vector and the length of L_n, respectively (see Fig. 3). Now, substitute eqns (23) and (31) into (59) and evaluate the integrals. We obtain

$$V_{ij}^S(\mathbf{x};\mathbf{s},a)=\frac{\mathrm{Im}}{\pi}\sum_{m=1}^{3}\left[\frac{A_{ij}(\eta_m)}{\hat{c}_\eta D(\eta_m)}\Theta_m^1(\mathbf{x};\mathbf{s},a)\right]+2aC_{ij}, \tag{60}$$

$$W_{ij}^S(\mathbf{x};\mathbf{s},a)=\frac{\mathrm{Im}}{\pi}\sum_{m=1}^{3}\left[\frac{B_{ij}(\eta_m)}{\hat{c}_\eta D(\eta_m)}\Theta_m^2(\mathbf{x};\mathbf{s},a)\right] \tag{61}$$

where

$$\Theta_m^1(\mathbf{x};\mathbf{s},a)=[z_m^+\log(z_m^+)-z_m^-\log(z_m^-)]/(\mathbf{d}_m\cdot\mathbf{s})-2a, \tag{62}$$

$$\Theta_m^2(\mathbf{x};\mathbf{s},a)=[\log(z_m^+)-\log(z_m^-)] \tag{63}$$

with

$$\mathbf{d}_m=\{1,\eta_m\}\quad\text{and}\quad z_m^\pm=\mathbf{d}_m\cdot(\mathbf{x}\pm a\mathbf{s}). \tag{64}$$

We note that in carrying out the integration, analyticity of the integrand has been assumed. Thus, when producing solutions for eqns (62) and (63), the branch of log (z) must be properly chosen such that the straight line connecting z_m^+ and z_m^- lies on a single sheet of $\log(z)$.

The results presented above do not include the singular case

$$H_{ij}^S(n,n)=W_{ij}^S(0;\mathbf{s},a)=PV\int_{a}^{a} h_{ij}^S(\mathbf{s}\xi;\mathbf{e})\,\mathrm{d}\xi\quad\text{at}\quad(\mathbf{s},a)=(\mathbf{s}_n,a_n).$$

A direct evaluation of the integral in the sense of Cauchy's principal value results in

$$H_{ij}^S(n,n)=0. \tag{65}$$

This result can also be obtained by observing that $h_{ij}^S(-\mathbf{x};\mathbf{e})=-h_{ij}^S(\mathbf{x};\mathbf{e})$ at $\mathbf{x}\neq 0$. Finally, we note that using straight line elements and constant spatial shape functions means $c_{ij}^n=\frac{1}{2}\delta_{ij}$, since at $\mathbf{x}_n$ the element is smooth.

4.3. *Evaluation of* $\mathbf{G}_k^R$ *and* $\mathbf{H}_k^R$

To obtain $G_{ij}^R(m,n,k)$ and $H_{ij}^R(m,n,k)$ defined by eqn (51) we also need to evaluate the time-convolution. We note that the time-convolutions in eqn (51) involve $\ddot{\varphi}_u$ and $\dot{\varphi}_t$. This suggests that we should choose the temporal shape function for the displacement one order higher than for the traction. Here, we consider the simplest case:

$$\varphi_u(t)=\frac{1}{\Delta t}[tH(t)-2(t-\Delta t)H(t-\Delta t)+(t-2\Delta t)H(t-2\Delta t)] \tag{66}$$

$$\varphi_t(t)=H(t)-H(t-\Delta t). \tag{67}$$

Thus, over each time-step the displacement is assumed to vary as a piece-wise linear function, while the traction is assumed constant.

Substituting eqns (18), (19), (57), (66) and (67) into eqn (51), we obtain

$$[G_{ij}^R(m,n;k), H_{ij}^R(m,n;k)] = [V_{ij}^R(\mathbf{x},t;\mathbf{s},a), W_{ij}^R(\mathbf{x},t;\mathbf{s},a)]$$
$$\text{at} \quad (\mathbf{x}=\mathbf{x}_n-\mathbf{x}_{mi}, t=t^k, \mathbf{s}=\mathbf{s}_n, a=a_n) \tag{68}$$

where

$$V_{ij}^R(\mathbf{x},t;\mathbf{s},a) = \int_0^t \int_{-a}^{a} g_{ij}^R(\mathbf{x}+\mathbf{s}\xi, t-\zeta)\dot{\phi}_t(\zeta)\,\mathrm{d}\xi\,\mathrm{d}\zeta, \tag{69}$$

$$W_{ij}^R(\mathbf{x},t;\mathbf{s},a) = \int_0^t \int_{-a}^{a} h_{ij}^R(\mathbf{x}+\mathbf{s}\xi, t-\zeta)\ddot{\phi}_u(\zeta)\,\mathrm{d}\xi\,\mathrm{d}\zeta. \tag{70}$$

Integrating with respect to ξ and ζ using eqns (18), (19), (66) and (67) yield

$$V_{ij}^R(\mathbf{x},t;\mathbf{s},a) = \frac{1}{4\pi^2}\int_{|\mathbf{n}|=1}\sum_{m=1}^{M}\frac{P_{ij}^m}{\rho c_m^2}\Psi_m^1(\mathbf{x},t)\,\mathrm{d}\mathbf{n} \tag{71}$$

$$W_{ij}^R(\mathbf{x},t;\mathbf{s},a) = \frac{1}{4\pi^2}\int_{|\mathbf{n}|=1}\sum_{m=1}^{M}\frac{Q_{ij}^m}{\rho c_m^3}\Psi_m^2(\mathbf{x},t)\,\mathrm{d}\mathbf{n} \tag{72}$$

where

$$\Psi_m^1(\mathbf{x},t) = \Psi_m(\mathbf{x},t)-\Psi_m(\mathbf{x},t-\Delta t), \tag{73}$$

$$\Psi_m^2(\mathbf{x},t) = [\Psi_m(\mathbf{x},t)-2\Psi_m(\mathbf{x},t-\Delta t)+\Psi_m(\mathbf{x},t-2\Delta t)]/\Delta t \tag{74}$$

in which

$$\Psi_m(\mathbf{x},t) = H(t)[(\chi_m^- \log|\chi_m^-|-\chi_m^+\log|\chi_m^+|)/(\mathbf{n}\cdot\mathbf{s})-2a], \tag{75}$$

$$\chi_m^{\pm} = c_m t+\mathbf{n}\cdot(\mathbf{x}\pm a\mathbf{s}). \tag{76}$$

In eqns (71) and (72) the integrals over the unit circle have to be computed numerically. The numerical integrations are easy to perform because the integrands are not singular functions. We note that in the integrands of eqns (71) and (72), $c_m(\mathbf{n})$ and $P_{ij}^m(\mathbf{n})$, defined by eqns (13) and (14), are independent of location and time. Thus they need to be computed only once for different elements and time-steps. The components $Q_{ij}^m(\mathbf{n},\mathbf{e})$ given by eqn (12) require some additional calculations. The only components in the integrands that have to be computed for each element and time-step are $\Psi_m^1(\mathbf{x},t)$ and $\Psi_m^2(\mathbf{x},t)$ given by eqns (73) and (74). These functions are rather simple and require little computational time. Since most numerical results can be repeatedly used for different elements and time-steps, our method is especially powerful for a large system with many elements and time-steps. Computations for $\mathbf{G}^S$, $\mathbf{H}^S$, $\mathbf{G}_k^R$ and $\mathbf{H}_k^R$ can be further reduced if we take into account that the material is undisturbed ahead of the wavefronts.

5. NUMERICAL EXAMPLES

Numerical computations have been carried out for the scattering of a plane transient wave by a cylindrical cavity in an unbounded solid. We first check the method by comparison of our results with existing solutions for a cavity in an isotropic solid. Then we present solutions for a transversely isotropic material. In all the cases, a circular cylindrical cavity of radius a is considered and the cylindrical boundary is divided into 48 elements

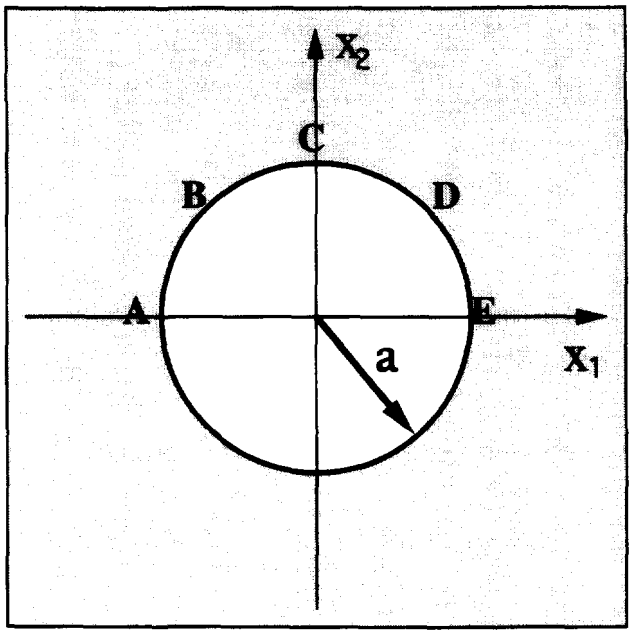

Fig. 4. Geometry of cylindrical cavity.

of equal size. The origin of the coordinate system is at the center point of the cavity (Fig. 4).

5.1. *Isotropic solid*

The isotropic solid considered is defined by $c_L/c_T = \sqrt{3}$ where c_L and c_T are the longitudinal and transverse wave velocities. The incident wave is chosen as

$$u_1^{in}(\mathbf{x}, t) = u_0[(c_L t - x_1 - a)/a]H(c_L t - x_1 - a)$$

which is a longitudinal plane wave propagating along the x_1-axis.

Scattering of a longitudinal wave by a circular cylindrical cavity in an isotropic solid has been solved analytically in the frequency domain by Pao and Mow (1973). The transient solutions have been produced by use of the fast Fourier transform. These transient solutions are used to check our numerical results.

The time increment has been taken as $c_T \Delta t/a = 0.12$. Figure 5 shows the displacements in the x_1-direction as functions of time at uniformly spaced points A, B, C, D, and E on the upper-half of the cylindrical boundary as shown in Fig. 4. Excellent agreement between our results (solid lines) and the analytical results of Pao and Mow (diamonds) can be observed.

5.2. *Transversely isotropic solid*

The x_1-axis is taken along the axis of symmetry (Musgrave, 1970). For a transversely isotropic solid the non-zero elastic constants are $c_{11} = c_{33}$, c_{22}, c_{13}, $c_{12} = c_{23}$, $c_{44} = c_{66}$, and $c_{55} = \frac{1}{2}(c_{33} - c_{13})$. Here c_{mn} is the shortened matrix notation for c_{ijpq} (Musgrave, 1970). As an example we consider a graphite-epoxy composite which has the following elastic constants $c_{11} = 160.7$, $c_{22} = 13.92$, $c_{12} = 6.44$, $c_{66} = 3.5$, and $c_{55} = 7.07$, in units of GPa.

Due to the material symmetry, incident plane waves propagating along the x_2-axis can be purely longitudinal or transverse waves. We consider a longitudinal incident wave in the form of a triangular pulse given by

$$u_2^{in}(\mathbf{x}, t) = (u_0/\delta)[p_1 H(p_1) - 2(p_1 - \delta)H(p_1 - \delta) + (p_1 - 2\delta)H(p_1 - 2\delta)], \qquad (77)$$

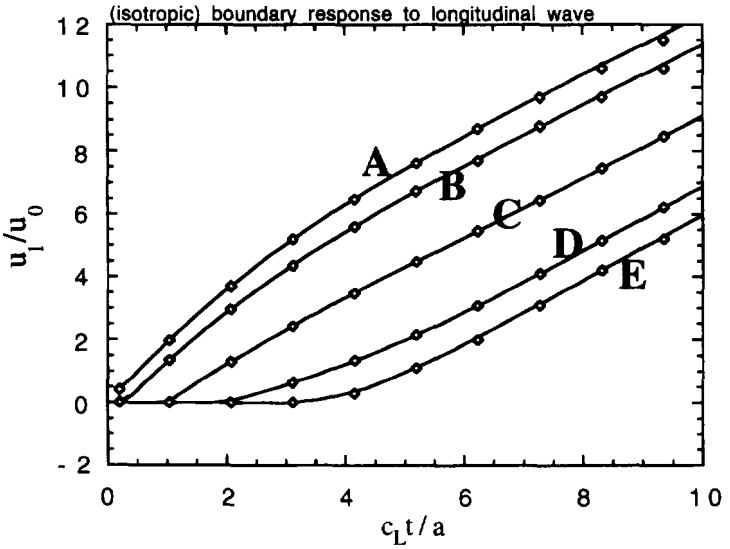

Fig. 5. Displacement on the surface of the cavity in an isotropic solid. Solid lines: solution of this paper. Diamonds: analytical solution.

with $u_1 = u_3 \equiv 0$, and an analogous transverse wave given by

$$u_1^{in}(\mathbf{x}, t) = (u_0/\delta)[p_2 H(p_2) - 2(p_2 - \delta)H(p_2 - \delta) + (p_2 - 2\delta)H(p_2 - 2\delta)] \tag{78}$$

with $u_2 = u_3 \equiv 0$. Here, $p_1 = t - c_1^{-1}(x_2 + a)$, $p_2 = t - c_2^{-1}(x_2 + a)$, $\delta = 0.25a$. The wave velocities are defined by $c_1/c_2 = 1.994$ and $c_2 = \sqrt{c_{66}/\rho}$. Equations (77) and (78) represent triangular pulses with u_0 as the height and 2δ as the base length of the triangle.

Graphite-epoxy composite is a strongly anisotropic material. The anisotropic properties of the material affect the velocity and wavefront curves, as shown in Fig. 6. The results are plotted in terms of the ratio to $\sqrt{c_{66}/\rho}$. Figure 6a shows that the velocity of pseudo longitudinal waves is the largest in the x_1-direction. The velocity of pseudo transverse waves increases in directions away from the x_1-directions, but then shows a significant dip in the x_2-direction. The concavity of the velocity curves in some ranges of the directions of wave propagation gives rise to the peculiar shapes of the wavefronts shown in Fig. 6b. In the x_1-direction the wavefronts are simple. The longitudinal wave arrives first and the transverse wave follows. Near the x_2-direction the significant differences at neighboring points in the velocities of pseudo transverse waves gives rise to the overlapping wavefronts. For wave motion that does not depend on x_3 in a transversely isotropic solid, the particle motion in the x_3-direction will not be generated, and hence the corresponding velocity and wavefront curves are not shown in Fig. 6. The velocity and wavefront curves help in interpreting the results. They also help in determining the time increment Δt, since Δt times the largest plane wave velocity must be small enough as compared to the length of the incident pulse and the size of the elements. In this computation, we found $\sqrt{c_{66}/\rho}\ \Delta t/a = 0.05$ to be satisfactory.

Figures 7 and 8 show images of scattered fields due to the presence of the cavity. Results of this type are of great interest in nondestructive evaluation where information on scattered waves is used to detect voids inside a material. The images are shown in gray scale which represents the amplitude of the displacement field. Shown in Fig. 7 are the scattered wave fields for the incident longitudinal pulse at times: $\tau = \sqrt{c_{66}/\rho}\, t/a = 0.05$, 0.25, 0.50, 0.75, 1.00, 1.25, 1.50, 2.00, and 2.50, respectively. Similarly, the scattered fields for the incident transverse pulse are plotted in Fig. 8. Figures 7 and 8 show that shortly after the incident wave hits the cavity, strong backscattered fields are generated together with weaker fields that are scattered to the sides. The sideways scattering is due to the higher longitudinal

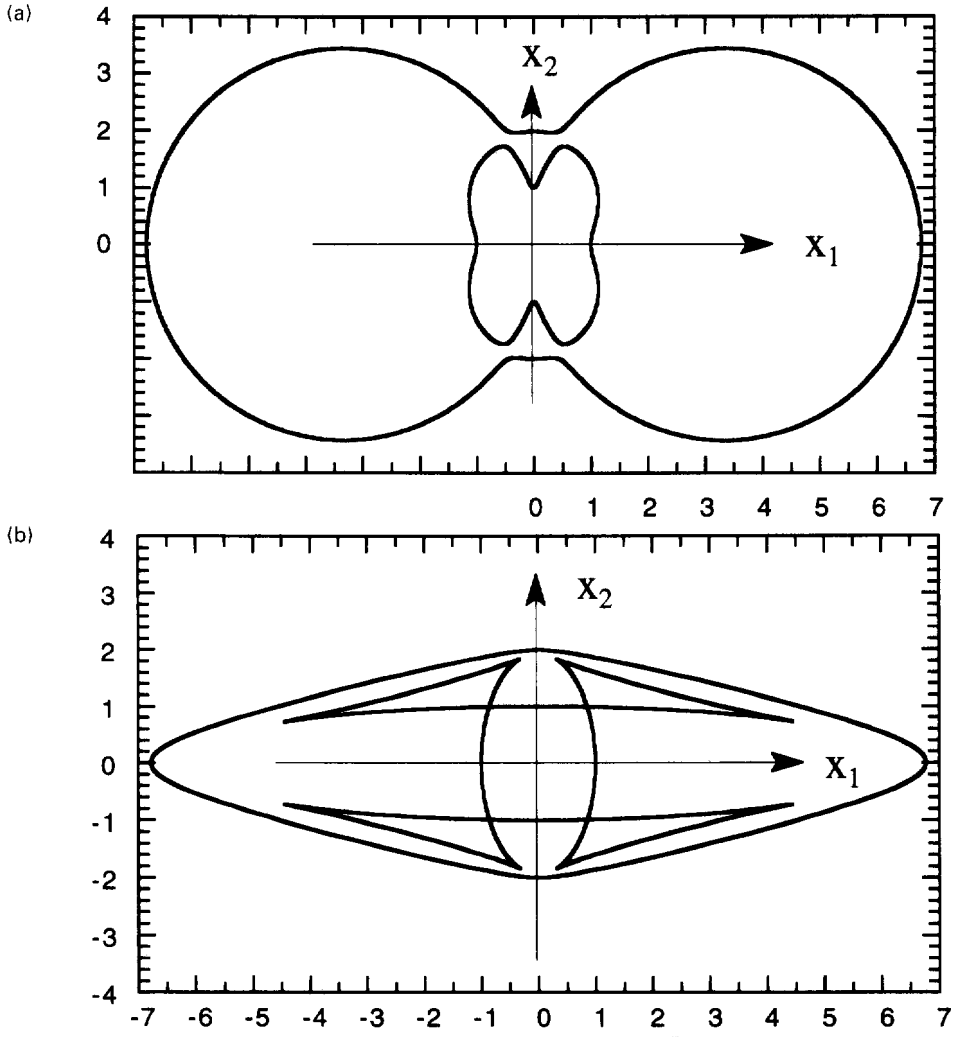

Fig. 6. (a) Plane wave velocity curves in terms of the ratio to $\sqrt{c_{66}/\rho}$. (b) Wavefronts corresponding to velocity curves.

wave speeds in the x_1-direction. The wavefronts are quite similar in shape to the wavefronts shown in Fig. 6b, including the presence of similarly shaped overlapping wavefronts. As the incident wave passes the cavity, scattered waves creep around the surface of the cavity while shedding wave motion into the surrounding material. For the incident longitudinal wave the shedding decreases temporarily when the midpoint of the cavity is passed, to pick up again when the creeping waves reach the back of the cavity. At that point the remaining creeping wave motion from both sides coalesces and generates a quite large signal which proceeds to propagate in the x_2-direction. Some creeping wave motion continues to propagate around the cavity. For the incident transverse wave the general pattern is quite similar except that the shedding of wave motion remains strong as the creeping waves pass the midpoint of the cavity. The coalescence of the creeping waves from both sides does not generate as strong a signal propagating in the x_2-direction, as is the case for the incident longitudinal wave.

Figures 9 and 10 show the scattered wave fields along a line above the cavity defined by $-5a \leqslant x_1 \leqslant 5a$ and $x_2 = 2a$. The results are plotted as functions of x_1 and dimensionless time τ. We see that near $x_1 = 0$ a large amplitude wave arrives first, particularly for the incident longitudinal pulse.

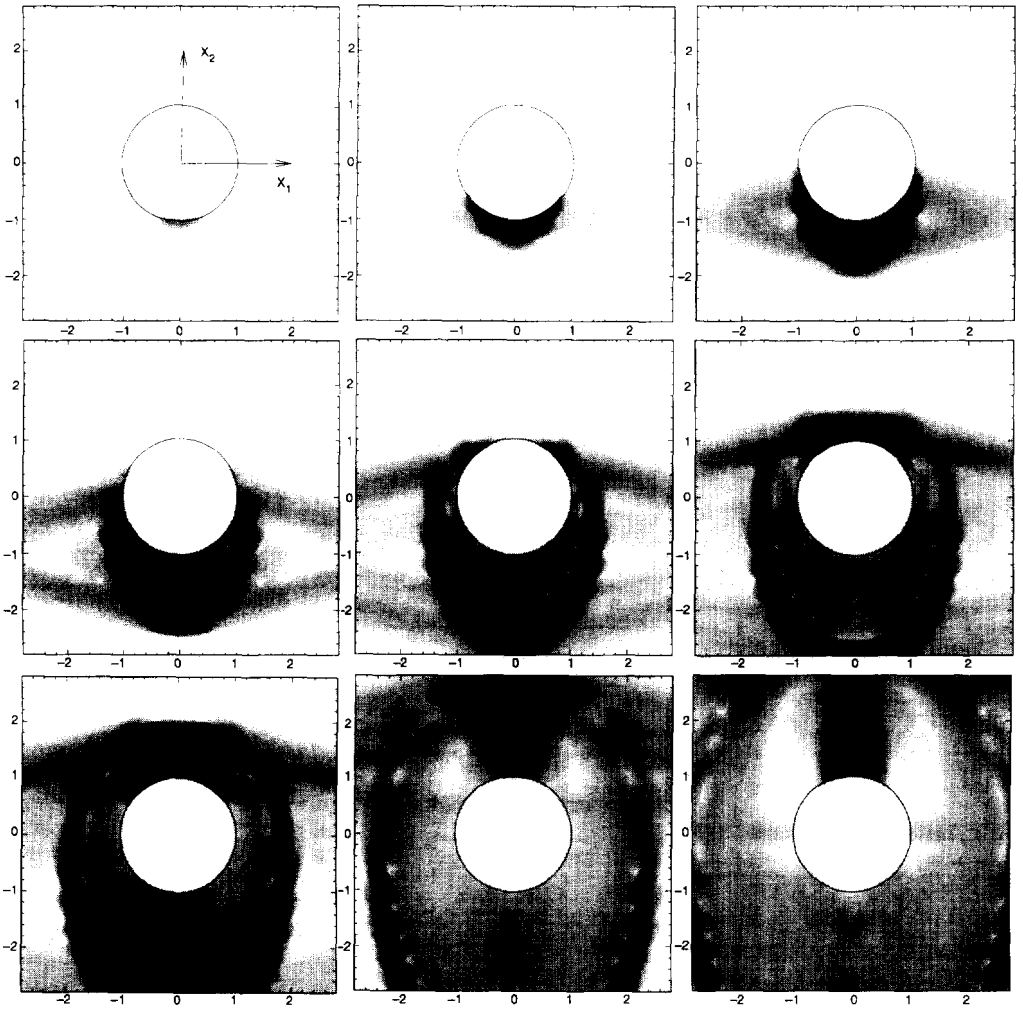

Fig. 7. Scattered wave field for plane longitudinal wave incident along the x_3-axis at times: $\tau = \sqrt{c_{66}}\, \rho\, t\, a = 0.05, 0.25, 0.50, 0.75, 1.00, 1.25, 1.50, 2.00$, and 2.50.

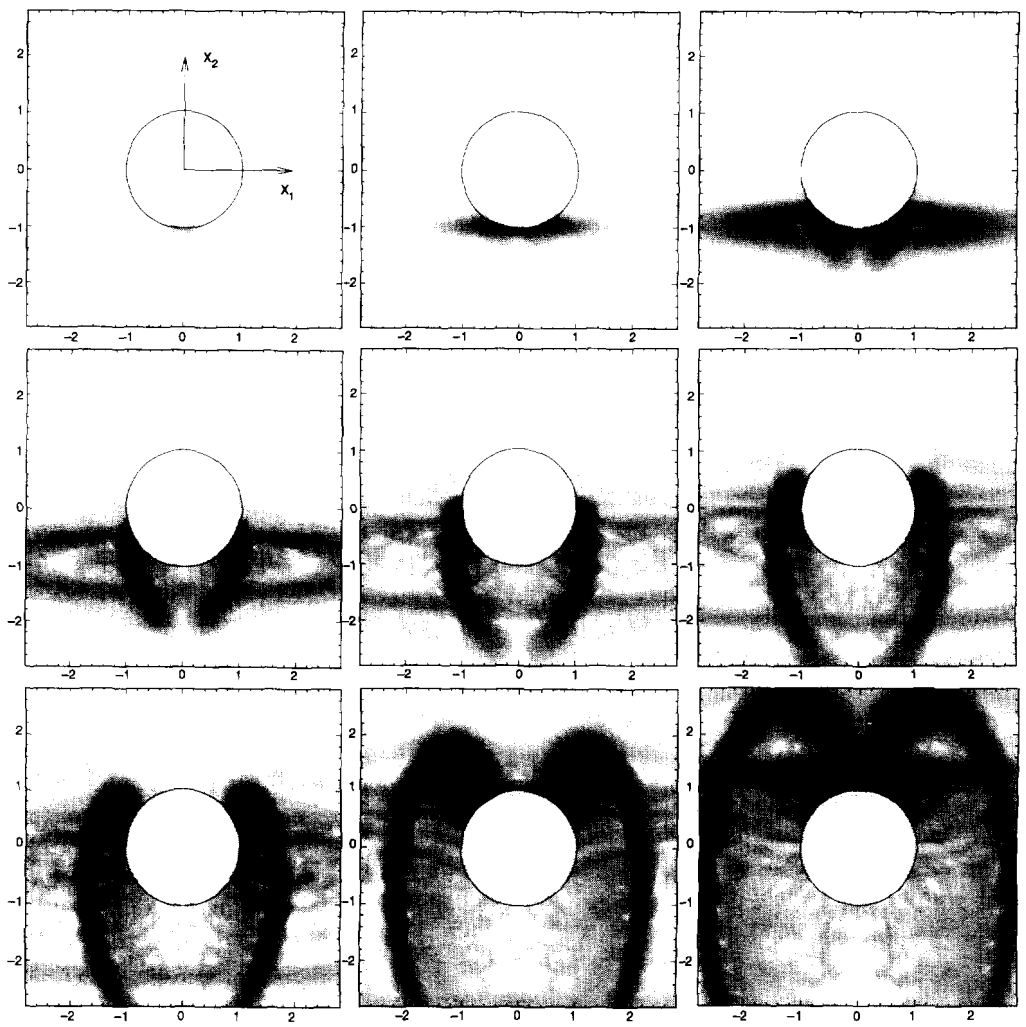

Fig. 8. Scattered wave field for plane transverse wave incident along the x_3-axis at times: $\tau = \sqrt{c_{66}/\rho}\, t/a = 0.05, 0.25, 0.50, 0.75, 1.00, 1.25, 1.50, 2.00$, and 2.50.

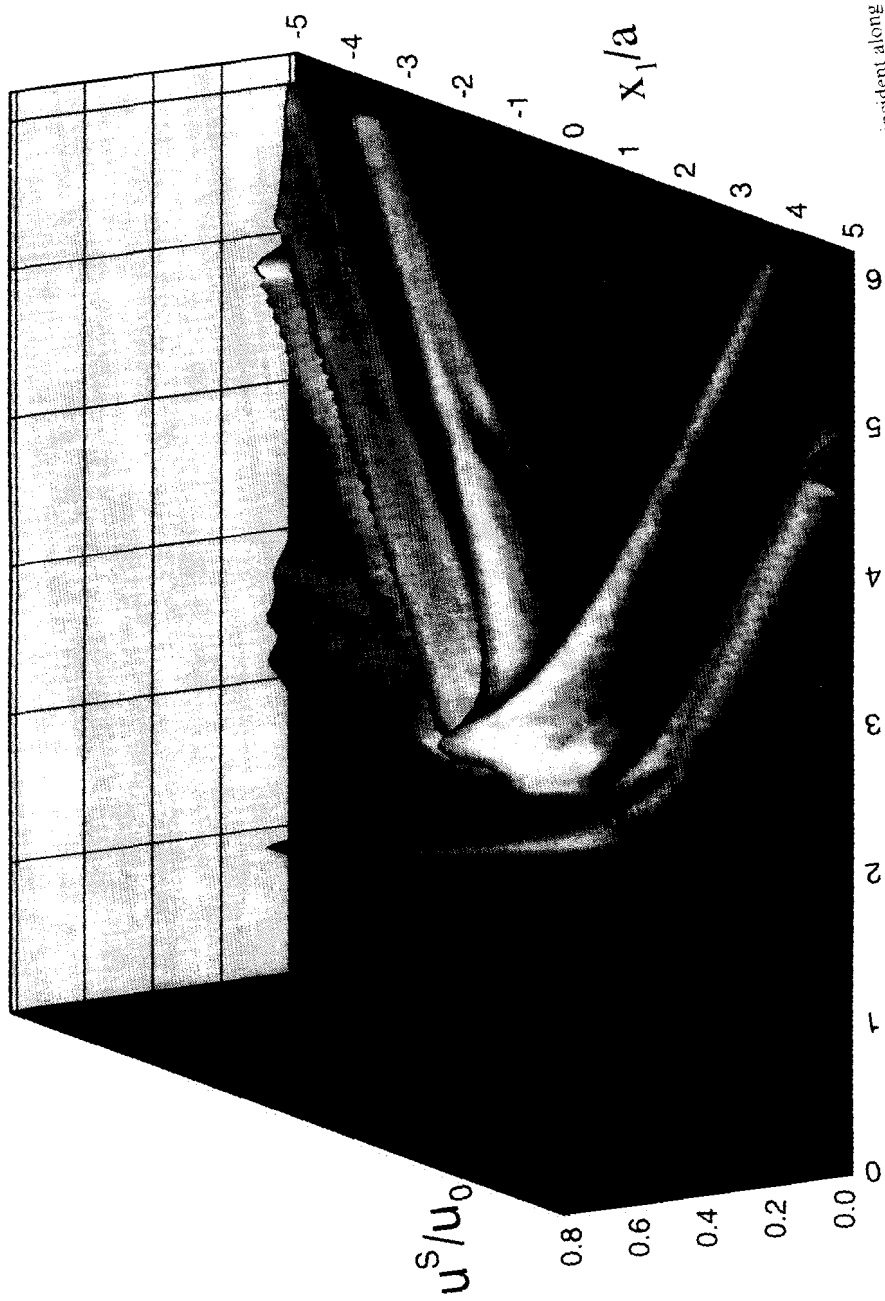

Fig. 9. Scattered wave fields along a line above the cavity defined by $-5a \leqslant x_1 \leqslant 5a$ and $x_2 = 2a$ for plane longitudinal wave incident along the x_2-axis.

Fig. 10. Scattered wave fields along a line above the cavity defined by $-5a \leqslant x_1 \leqslant 5a$ and $x_2 = 2a$ for plane transverse wave incident along the x_2-axis.

The real advantage of the BEM over other numerical methods is the capability to produce accurate numerical solutions at specified points in the material without carrying out calculations for the whole domain. This is extremely attractive in applications to nondestructive evaluation where frequently the measurement is carried out over a small area. The method developed in this paper has the potential to provide computer simulation of a real testing situation in a very convenient way.

6. CONCLUDING COMMENTS

An efficient algorithm for two-dimensional time-domain Boundary Element Method has been developed to solve elastodynamic boundary/initial-value problems in solids of general anisotropy. The integral expressions for the Green's functions derived by Wang and Achenbach (1994) are decomposed into singular static and regular dynamic parts. The singular static parts, eqns (23), (31) and (32), correspond to the elastostatic Green's functions. The regular dynamic parts, eqns (18) and (19), are given in terms of line integrals over a unit circle. By analytically evaluating the integration over each boundary element and the time-convolution over each time-step, the numerical computations reduce to an extent that the computational time for general anisotropy is close to or even less than that required by conventional BEM for isotropic materials. In the construction of the element matrices, only regular line integrals over the unit circle have to be computed numerically. Numerical calculations for scattering of elastic waves by a circular cylindrical cavity have been carried out for an isotropic solid and a graphite-epoxy composite. Numerical results for the isotropic solid agree well with the analytical solutions. Calculations for the graphite-epoxy composite have shown some interesting phenomena of the scattered wave fields in an anisotropic solid. This paper has demonstrated that the Boundary Element Method can be efficiently applied to solve dynamic problems in solids of general anisotropy.

Acknowledgements—This work was partially supported by the Office of Naval Research under Contract N00014-89-J-1362, and partially by the Science and Technology Agency of Japan.

REFERENCES

Achenbach, J. D. (1993). *Wave Propagation in Elastic Solids*, North-Holland-Elsevier, Amsterdam.
Barnett, D. M. and Lothe, J. (1973). Synthesis of the sextic and the integral formalism for dislocation, Green's functions and surface waves in anisotropic elastic solids. *Phys. Norv.* **7**, 13–19.
Chen, G. and Zhou, J. (1992). *Boundary Element Methods*, Academic Press, London.
Cruse, T. A. (1988). *Boundary Element Analysis in Computational Fracture Mechanics*, Kluwer Academic Publishers, Dordrecht.
DiNicola, A. J. (1994). Fundamental tensors for the boundary element method with general three-dimensional elastic anisotropy. In *Boundary Element Technology IX* (eds Brebbia, C. A. and Kassab, A. J.) Computational Mechanics Publications, Southampton, Boston, pp. 261–270.
Fellinger, P., Marklein, R., Langenberg, K. J. and Klaholz, S. (1995). Numerical modeling of elastic wave propagation and scattering with EFIT—elastodynamic finite integration technique. *Wave Motion* **21**, 47–66.
Hwu, C. and Yen, W. J. (1991). Green's functions of two-dimensional anisotropic plates containing an elliptic hole. *Int. J. Solids Structures* **27**, 1705–1719.
Kane, J. H. (1994). *Boundary Element Analysis in Engineering Continuum Mechanics*, Prentice Hall, Englewood Cliffs.
Kitahara, M., Hirose, S. and Achenbach, J. D. (1992). Transient elastodynamic analysis for three-dimensional configurations. In *Advanced Dynamic Analysis by Boundary Element Methods* (eds Banerjee, P. K. and Kobayashi, S.) Elsevier, New York, pp. 253–281.
Manolis, G. D. and Beskos, D. E. (1988). *Boundary Element Methods in Elastodynamics*, Unwin Hyman, London.
Musgrave, M. J. P. (1970). *Crystal Acoustics*, Holden-Day, Inc., San Francisco.
Pao, Y.-H. and Mow, C. C. (1973). *Diffraction of Elastic Waves and Dynamic Stress Concentrations*, Crane & Russak, New York.
Stroh, A. N. (1958). Dislocations and cracks in anisotropic elasticity. *Phil Mag.* **3**, 625–646.
Ting, T. C. T. (1992). Image singularities of Green's functions for anisotropic elastic half-spaces and bimaterials. *Q. J. Mech. Appl. Math.* **45**, 120–139.
Vogel, S. M. and Rizzo, F. J. (1973). An integral equation formulation of three-dimensional anisotropic elastostatic boundary value problems. *J. Elasticity* **3**, 203–216.
Wang, C.-Y. (1994). 2-D elastostatic Green's functions for general anisotropic solids and generalization of Stroh's formalism. *Int. J. Solids Structures* **31**, 2591–2597.
Wang, C.-Y. (1995). 3-D elastostatic Green's tensors in anisotropic crystals. Submitted.

Wang, C.-Y. and Achenbach, J. D. (1992). A new look at 2D time-domain elastodynamic Green's functions for general anisotropic solids. *Wave Motion* **16,** 389–405.

Wang, C.-Y. and Achenbach, J. D. (1994). Elastodynamic fundamental solutions for anisotropic solids. *Geophys. J. Int.* **118,** 384–392.

Wang, C.-Y. and Takemiya, H. (1992). Analytical elements of time domain BEM for two-dimensional scalar wave problems. *Int. J. Num. Methods Engng* **33,** 1737–1754.

Wilson, R. B. and Cruse, T. A. (1978). Efficient implementation of anisotropic three-dimensional boundary integral equation stress analysis. *Int. J. Num. Methods Engng* **12,** 1383–1397.